



Investigating the wear performance of AZ91D magnesium composites with ZnO, MnO, and TiO₂ nanoparticles

Annamalai Gnanavelbabu¹ · Elayarasan Vinothkumar¹ · Nimel Sworna Ross² · Muthu Prahadeeswaran¹

Received: 10 August 2023 / Accepted: 9 October 2023 / Published online: 4 November 2023
© The Author(s) 2023

Abstract

In recent decades, there has been a notable advancement in the field of bioactive, biodegradable, and biocompatible metallic materials, particularly for applications in general surgery. Among these materials, magnesium alloy-based composites have gained popularity due to their excellent biological properties and adequate strength. However, their resistance to wear is still an area that requires further investigation. Therefore, this study examines the wear properties of stir-ultrasonic-squeeze-casted magnesium (AZ91D) composites, incorporating distinct nanoparticles such as ZnO, MnO, and TiO₂. The Evaluation-based Distance from Average Solution (EDAS) approach is used to determine the optimal parameters. Additionally, an Analysis of Variance (ANOVA) is conducted to identify the crucial factors influencing the responses. The effect of process factors on the wear rate and Coefficient of Friction (COF) is then investigated using response surface plots. The confirmation assessments reveal that the optimal parameter conditions for the tribo process comprise a 50.0018 N applied load, a 1.4998 m/s sliding velocity, and the AZ91D + 1% TiO₂ (ATO) composite utilization. The ANOVA findings demonstrate that the applied load significantly contributes to 67.3% of the wear performance. Subsequently, after determining the optimal condition, it is observed that the ATO composite, when exposed to temperatures above 150 °C, exhibits an abrupt increase in wear rate and COF due to the degradation of grain strength and the dissolution of the β-phase within the composite.

Keywords Biocompatible · Tribometer · EDAS-RSM · Optimization · Nanocomposites

1 Introduction

Metallic materials, such as titanium (Ti), stainless steel (SS), and cobalt-chromium (Co-Cr) alloys, are highly desired in biomedical applications due to their superior overall performance [1, 2]. However, the need for secondary surgery to remove these bio-inert implants after tissue recovery causes physical discomfort and patient morbidity. The solution lies in developing biodegradable implants that can eliminate the requirement for retraction; one major disadvantage of conventional materials is their considerably higher elastic

modulus when compared to that of natural bones. This discrepancy leads to a stress-shield effect, impeding the natural growth of new bone tissue [3, 4]. To address these challenges, Magnesium (Mg) has gained considerable attention as a promising alternative because of its good biocompatibility and relatively low elastic modulus [5, 6]. AZ series alloy is commonly used in Mg alloy because of its low cost, superior casting qualities, and appropriate mechanical properties [7–9]. With an elastic modulus of approximately 45 GPa, Mg and its alloys effectively mitigate the stress-shielding effect, distinguishing them from conventional metallic orthopedic implants like SS (189–205 GPa), Co-Cr alloys (230 GPa), and Ti alloys (105–117 GPa). Natural bone, on the other hand, exhibits an elastic modulus ranging from approximately 3 to 20 GPa [10, 11]. However, the main disadvantages of Mg and its alloys are their poor strength at both low and high temperatures, as well as their poor resistance to wear. Wear is the main problem among these, which reduces the lifespan of parts made of Mg and makes it unsuitable for various biomedical applications.

✉ Nimel Sworna Ross
nimelross@gmail.com

Annamalai Gnanavelbabu
dr.agbabu@gmail.com

¹ Department of Industrial Engineering, CEG Campus, Anna University, Chennai 600025, India

² Department of Mechanical and Industrial Engineering Technology, University of Johannesburg, Johannesburg, South Africa

To increase the wear resistance of Mg composites, reinforcement elements including carbides, nitrides, borides, and oxides are frequently utilized [12]. Particularly, in the oxide family, nano-oxide reinforcements like ZnO, MnO, and TiO₂ improve mechanical and tribological characteristics [13–15]. Selvam et al. examined the tribological properties of Mg-nZnO nanocomposites and found that adding nano-ZnO particles to the Mg matrix increases wear resistance by forming thick oxide layers during sliding [16]. AZ31-ZnO composite was studied using suction casting to investigate grain refinement and mechanical characteristics. Results showed that adding ZnO particles improved yield strength and Ultimate Tensile Strength (UTS) by 206 and 66 MPa, respectively, by limiting grain growth and restricting nucleation via microconvection [17]. Panchal and Rao studied the microstructure and mechanical characteristics of Al-MnO₂ composites and discovered that the emergence of new phases like MnAl₆ and Mn₃AlC at the grain boundary improves all mechanical properties like hardness, UTS, and percent of elongation [18]. An LM13 Al hybrid composite containing 12% TiO₂ and 3% MoS₂ was studied for its tribological properties with varying load, velocity, and distance. Results showed that higher load and velocity led to increased wear and a change in wear mechanism, while longer sliding distance resulted in reduced wear. Additionally, the composite had less volume loss than alloys, due to the TiO₂ and MoS₂ additions [19]. When compared to the matrix alloy, Al6061-xTiO₂ (2, 4, 6, 8, 10) composites had high hardness and a low wear coefficient. The volumetric wear loss increased with increased loads and sliding distances, whereas the wear coefficient decreased for alloy and its composites. However, Al6061-8wt.% TiO₂ had a low wear coefficient under the same test conditions [20]. Alagarsamy and Ravichandran studied the mechanical and tribological behavior of AA7075-xTiO₂ composites (0, 5, 10, 15%) and found that up to 10% TiO₂ reinforcement improved mechanical and wear resistance. However, increasing the reinforcement to 15% resulted in decreased properties due to agglomeration [21].

Metal matrix composite (MMC) characteristics are affected by many parameters, including the base material, reinforcement size, composition, and fabrication process [22]. Generally, a variety of techniques, including stir and squeeze casting, powder metallurgy, and spray forming, are utilized to fabricate MMC [23, 24]. Stir-squeeze casting is a popular process for MMC production, but long stirring causes oxidation and agglomeration leading to poor casting and porosity. To fix this, ultrasonic treatment (UST) was used to quickly and evenly mix reinforcement into the matrix through ultrasonic vibration. Squeeze casting has benefits over conventional casting, such as reduced porosity, refined grain structure, and improved mechanical characteristics

[25]. As a result, the stir-UST-squeeze casting technique is commonly employed to enhance the microstructure properties and mechanical strength of composites [26]. T6 heat treatment successfully enhances the strength of the AZ91D Mg alloy by regenerating β -Mg₁₇Al₁₂ particles, which decreases the rate of wear [27]. Shah et al. analyzed the effect of artificial age hardening treatment (T6) on Al-Si-Mg alloy at various aging temperatures (150, 170, 190, 210, and 230 °C). The results indicate that an increase in aging temperature revealed a continuous reduction in the wear rate due to the refinement of eutectic silicon particles [28].

Several optimization tools are used to optimize the tribological characteristics of the composites; the Technique for Order of Preference by Similarity to Ideal Solution (TOPSIS) method supersedes the EDAS method in terms of computation methods. Here, the positive (PDA) and negative distances (NDA) of all the responses were computed from the average value rather than using Euclidean distances. Based on the normalized weighted sums of these distances, the solutions are rated from best to worst [29]. Chairman et al. optimized the TiO₂ filler wt% to enhance the mechanical and wear characteristics of polymer composites reinforced by woven glass fiber and discovered that 2 wt.% of filler is the optimum value for tensile, compression, interlaminar shear strength, impact strength, and wear rate [30]. Madhukar et al. used the Taguchi technique to investigate the pin-on-disc process parameter (load, sliding velocity, and distance) on the tribological behavior of AA7150-hBN composites. They concluded that COF and wear rate are strongly influenced by the applied load [31]. Singh and Chauhan analyzed the impact of various process variables on the wear performance of AZ91D/B₄C composites using ANOVA. The optimum condition was observed at 10 N load, 1.0 m/s of sliding speed, and 1000 m of sliding distance [32]. Rajmohan et al. successfully applied Taguchi L₉ orthogonal array-gray fuzzy algorithms to optimize specific wear rate and COF of Mg-SiC composites [33].

From the literature survey, the addition of metal oxide particles into the matrix is predicted to serve as a load carrier and dislocation barrier by developing a thick oxide film on the metal substrate that minimizes the wear rate and material removal rate, and our findings support this hypothesis. However, there is a limited research article on oxide particles to enhance the tribological properties of Mg composites. Particularly, optimization study on the wear properties of metal oxide reinforced Mg nanocomposites. Therefore, the focus of the current work is to use an EDAS technique to analyze and identify the optimum wear conditions for metal oxide-reinforced AZ91D nanocomposites. The wear test was conducted using a pin-on-disc tribometer with an L₃₆ orthogonal array and three distinct process variables like applied load (50–100 N), sliding velocity (0.5–1.5 m/s), and

materials (AZD, AZO, AMO, and ATO). The wear rate and COF are the two responses. The optimal process parameter was determined using the EDAS-RSM approach. Desirability and confirmation tests were used to confirm the optimum condition.

2 Experiment and methodology

2.1 Materials

In this research, AZ91D Mg alloy supplied by Exclusive Magnesium (India) was utilized as a base matrix material. Table 1 shows the chemical composition of AZ91D Mg alloy. Nanoparticles of ZnO, MnO, and TiO₂ were utilized as reinforcement particles for the fabrication of nanocomposites. Table 2 displays the physical characteristics of Mg alloy and oxide particles. The details of specimen code used for different nanocomposites and their compositions are displayed in Table 3.

2.2 Fabrication process of MMC

Mg is a highly reactive element that reacts with its environment to produce magnesium oxides (MgO). So specially designed ultrasonic-assisted bottom pouring stir squeeze casting furnace with protective environment was used in the fabrication of alloy and nanocomposites. One kilogram of AZ91D rod was cut into 50 mm×50 mm×20 mm billets using an abrasive cutter. The AZ91D billets were kept inside the furnace at 800 °C to convert them into a complete liquidus state. A protective gas atmosphere was developed by supplying Ar and SF₆ in the ratio of 9:1 to avoid the formation of MgO.

The melted metal was stirred at 400 rpm for 5 min. using a graphite-coated stirrer. Simultaneously, the oxide reinforcements were preheated in a muffle furnace at 300 °C for 1 h to remove moisture content in the particles. The Ti-made ultrasonic probe was inserted into the molten metal and controlled using a controller to maintain vibration at 2.5 kW power and 20,000 Hz frequency for 5 min. The ultrasonic process reduces reinforcement agglomeration and makes an even dispersion of particles in the composites. The fabrication setup is shown in Fig. 1. Then, the molten metal is poured into a die with a temperature of 300 °C and dimensions of $\Phi 50 \times 1300$ mm through a 750 °C preheated runway. Simultaneously, squeezing was done on the melted for 2 min at 150 MPa to reduce the porosity in the final product.

Table 1 Constituent elements of AZ91D

Elements	Aluminium	Zinc	Manganese	Silicon	Iron	Nickel	Copper	Magnesium
%	9.100	0.850	0.150	0.050	0.005	0.002	0.003	Bal.

Table 2 Physical properties of Mg matrix and oxide reinforcements [25]

Materials	Density (g/cc)	Melting Point (°C)	CTE (K ⁻¹)
AZ91D	1.81	595	26×10 ⁻⁶
ZnO	5.60	1974	6.5×10 ⁻⁶
MnO	5.43	1945	9.3×10 ⁻⁶
TiO ₂	4	1843	9×10 ⁻⁶

Table 3 Details of the composition and their specimen code

S. No.	Composition				Specimen Code
	AZ91D	ZnO	MnO	TiO ₂	
1	100%	-	-	-	AZD
2	99%	1%	-	-	AZO
3	99%	-	1%	-	AMO
4	99%	-	-	1%	ATO

2.3 Heat treatment process

The heat treatment process was conducted as per the ASTM B661-06 standard in a muffle furnace with a constant argon supply to prevent oxidation of alloy and composite. Initially, the specimen was heated from ambient temperature to 415 °C and maintained for 16 h (solutionizing) with a temperature rise of 1.5 °C/min. approximately. After that, the specimen was water quenched. Finally, aging was carried out for 16 h at a temperature of 168 °C and air-cooled at room temperature. The graphical illustration of a heat treatment process is shown in Fig. 1.

2.4 Pin-on-disc wear test

The wear test was conducted on fabricated materials using a pin-on-disc tribometer (DUCOM, India) at dry and elevated conditions as shown in Fig. 2. EN 31 hardened steel was used as a counter disc with a hardness of 65 HRC. For this testing, a cylindrical pin-shaped specimen was cut with a dimension of $\varnothing 8$ and a length of 32 mm. The mass of the sample was measured before and after the test using an electronic weighing balance (accuracy, 0.01 mg). A dry wear test was conducted with varying loads (50, 75, 100 N), varying sliding speeds (0.5, 1.0, 1.5 m/s), and constant distance (1000 m). The elevated temperature test was carried

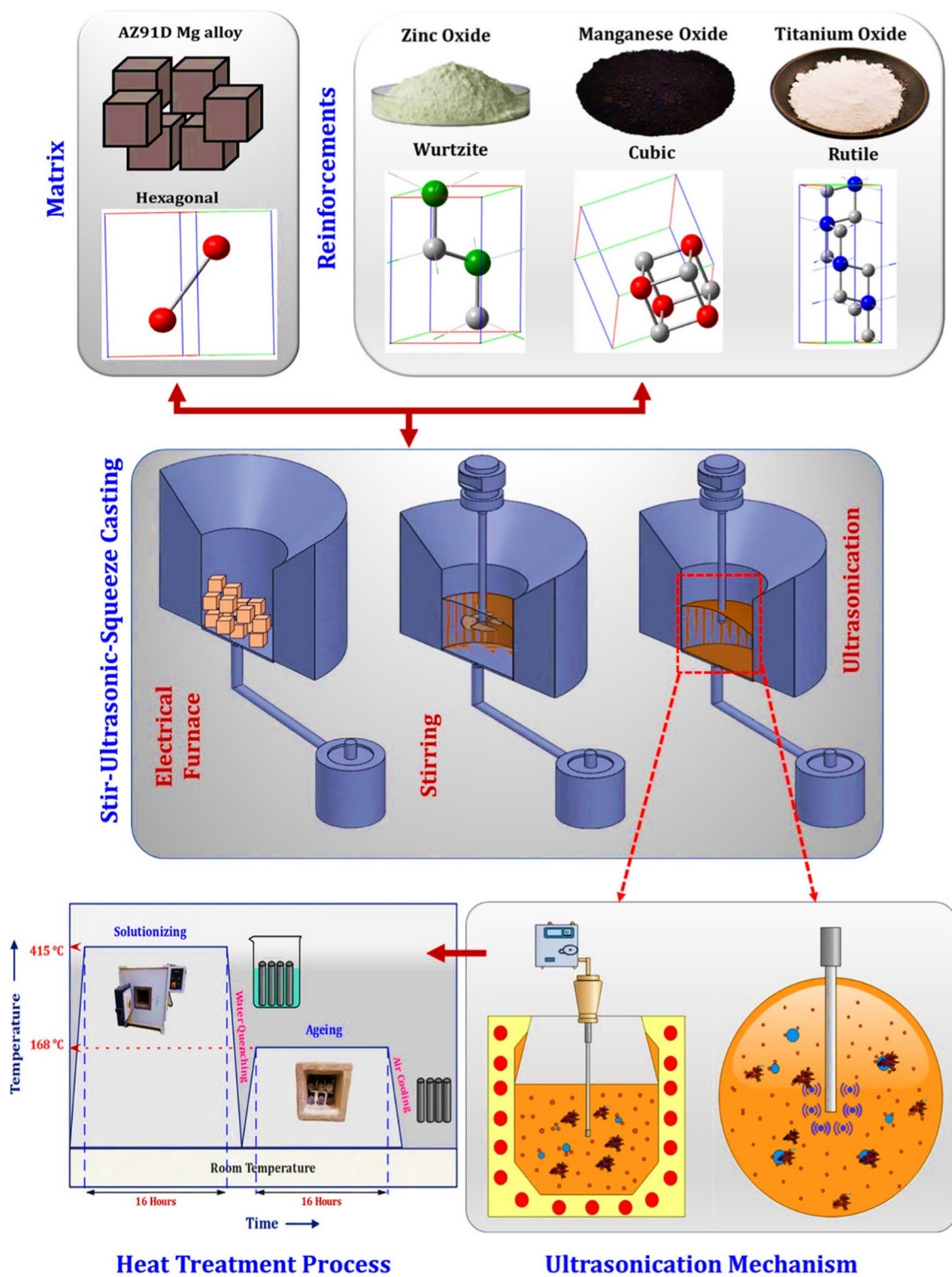


Fig. 1 Schematic illustration for fabrication of nanocomposites

out at optimum process parameter (load, sliding velocity, and material) conditions under varying temperatures (50, 100, 150, and 200 °C). A small hole (\varnothing 2 mm) was made on one side of the pin surface for inserting the thermocouple

to monitor the testing temperature. Both before and after the test, the sample was cleaned with acetone. Eq. 1 was used to determine the wear rate, and DUCOM software was used to determine the COF.

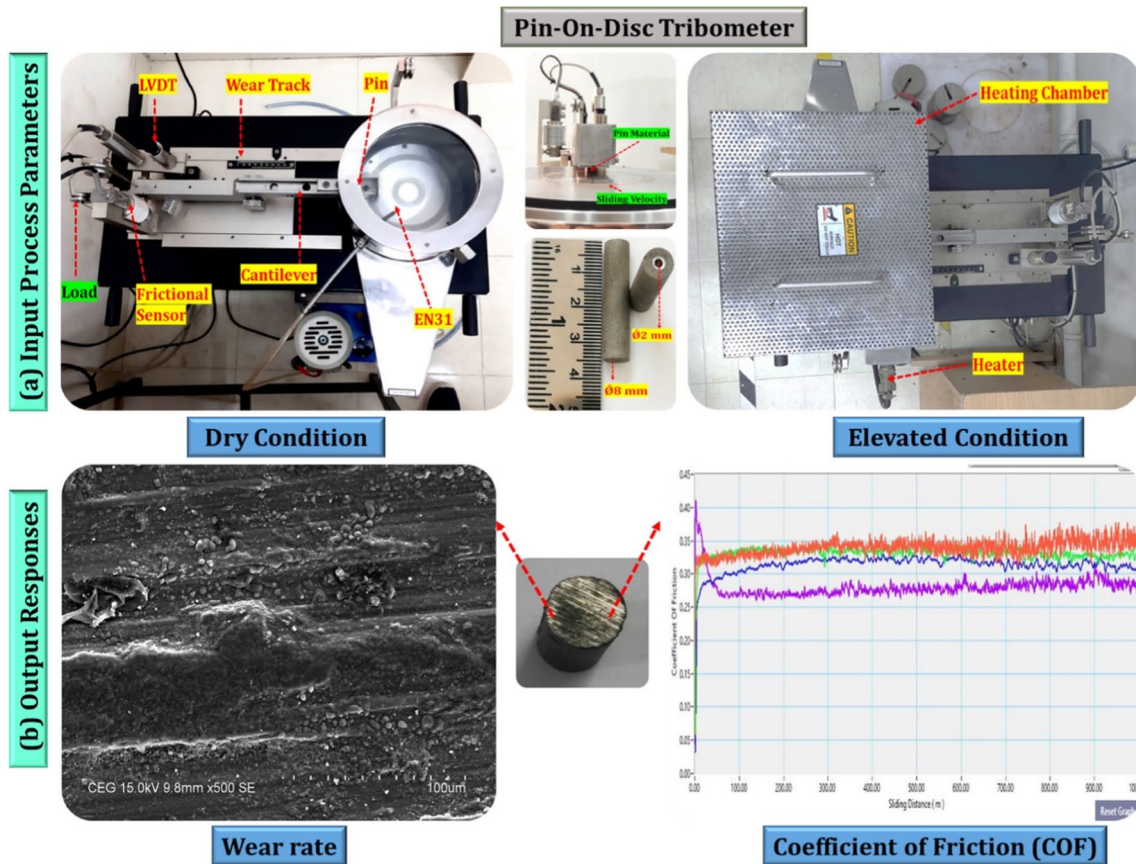


Fig. 2 (a-b). Pin-on-disc tribometer (a) Input parameters, (b) Output responses

$$\text{Wear rate} = \frac{\text{Mass before test} - \text{Mass after test}}{\text{Sliding Distance}} \text{ (mm}^3/\text{m)} \tag{1}$$

2.5 EDAS-RSM methodology

To study the impact of pin-on-disc tribometer process variables on the tribological behavior of Mg nanocomposites. The three major process variables and their levels are displayed in Table 4. Wear rate and COF were responses for the process. It is preferred to be “smaller the better.” The EDAS and RSM methodology was used to identify the optimal condition. The maximum EDAS grade value was

considered a best process parameter condition. An RSM-derived polynomial model that connects the process variables to the EDAS grade value was developed. Desirability and confirmation tests were also used to confirm the optimum results. The steps which we followed to optimize the process variables are illustrated in Fig. 3.

Step 1: The average value of each response was calculated using Eq. 2 (AV_j)

$$AV_j = \frac{\sum_{i=1}^n x_{ij}}{n} \tag{2}$$

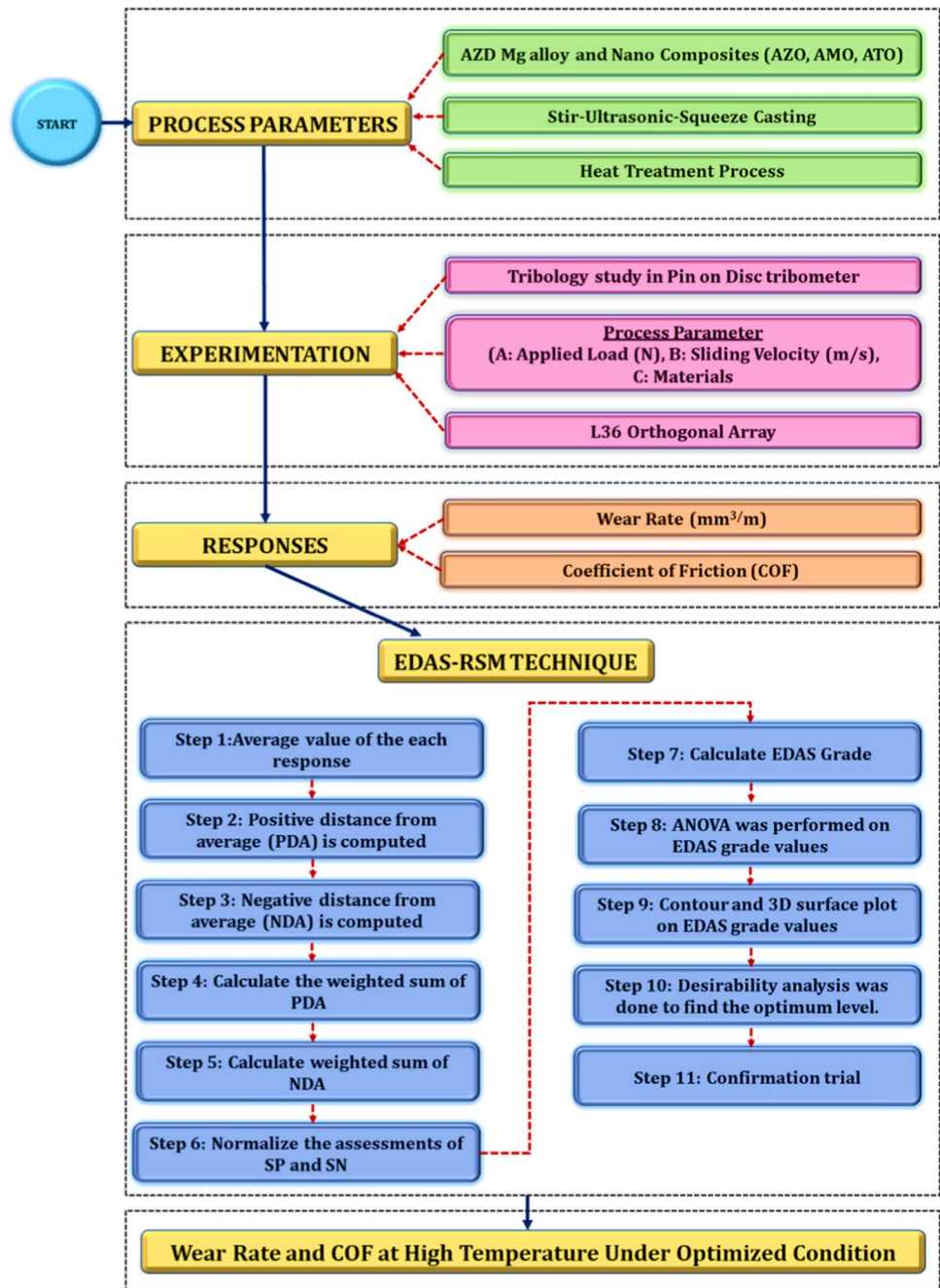
where x_{ij} is the response value and n is the total no. of values.

Step 2: The PDA is calculated by non-beneficial conditions using Eq. 4

Table 4 Process variables and levels for dry sliding wear

S. No.	Process Variables	Unit	L1	L2	L3	L4
1	Applied load (A)	N	50	75	100	-
2	Sliding velocity (B)	m/s	0.5	1	1.5	-
3	Materials (C)		AZD	AZO	AMO	ATO

Fig. 3 Illustration of steps of EDAS-RSM technique



$$PDA_{ij} = \frac{\max(0, (x_{ij} - AV_j))}{AV_j} \text{ (beneficial)} \tag{3}$$

$$NDA_{ij} = \frac{\max(0, (AV_j - x_{ij}))}{AV_j} \text{ (beneficial)} \tag{5}$$

$$PDA_{ij} = \frac{\max(0, (AV_j - x_{ij}))}{AV_j} \text{ (non - beneficial)} \tag{4}$$

$$NDA_{ij} = \frac{\max(0, (x_{ij} - AV_j))}{AV_j} \text{ (non - beneficial)} \tag{6}$$

Step 3: The NDA is calculated by non-beneficial conditions using Eq. 6

Step 4: The weighted sum of PDA was calculated using Eq. 7

$$SP_i = \sum_{j=1}^n w_j PDA_{ij} \tag{7}$$

Step 5: Weighted sum of NDA is calculated using Eq. 8

$$SP_i = \sum_{j=1}^n w_j NDA_{ij} \tag{8}$$

The values of the weights (W_j) are 0.5.

Step 6: Normalized the SP and SN values using Eqs. 9 and 10

$$NSP_j = \frac{SP_i}{\max_i (SP_i)} \tag{9}$$

$$NSN_j = 1 - \frac{SN_i}{\max_i (SN_i)} \tag{10}$$

Step 7: Calculation of EDAS grade and the average value of NSP and NSN was considered as EDAS grade using Eq. 11.

$$EDAS\ Grade = \frac{NSP_i + NSN_j}{2} \tag{11}$$

Step 8: Perform an ANOVA to determine the model’s suitability and the significant process variables, along with their interactions.

Step 9: Create contour and 3D surface plots to examine the impact of specific process variables on EDAS grade value.

Step 10: A desirability study was conducted to determine the optimal level of process variables.

Step 11: A confirmation assessment was performed to validate the EDAS-RSM accuracy from the maximum EDAS grade value.

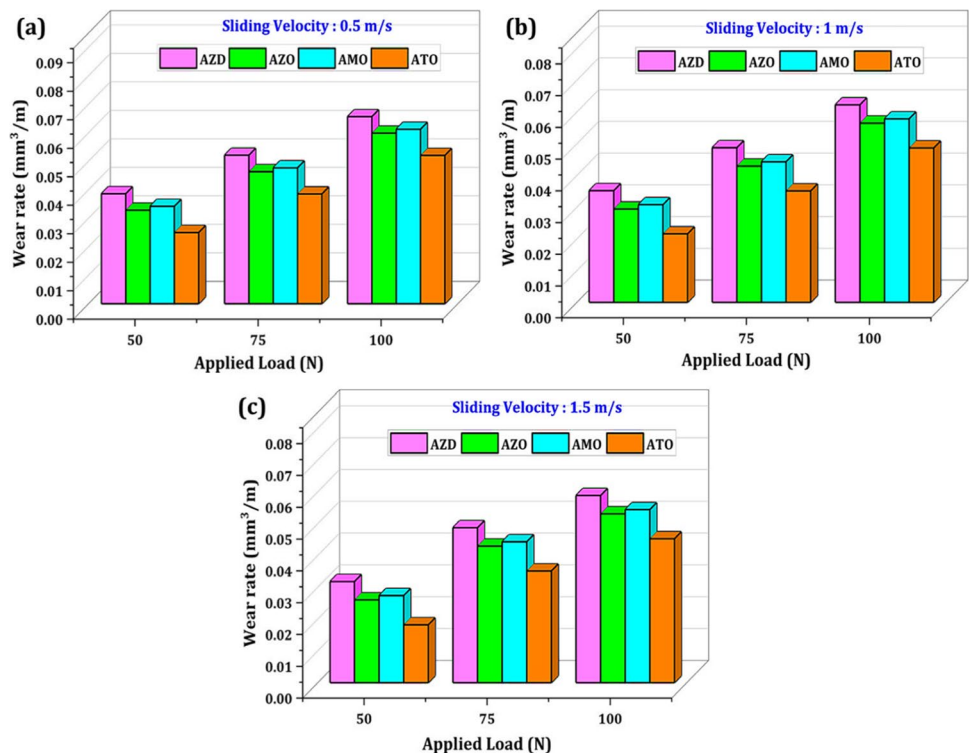
3 Results and discussion

3.1 Effect of load on wear rate and COF of the materials

For analyzing the effect of oxide reinforcements, a pin-on-disc tribo test was done on the produced Mg alloy (AZD) and nanocomposites (AZO, AMO, and ATO). The wear rate and COF of the materials have been investigated at different levels of “A” (ranging from 50 N to 100 N) across three distinct sets of “B” (ranging from 0.5 m/s to 1.5 m/s), under constant sliding distance (1000 m). Similarly, the wear and friction behavior of the materials at various “B’s” (0.5, 1.0, and 1.5 m/s) have also been examined for the three distinct sets of “A’s” (50, 75, and 100 N).

Figure 4(a–c) shows the wear rate of fabricated alloy and nanocomposites at different “A’s” (50, 75, and 100 N). The mass loss method was used to determine the influence of “A” on the wear rate of materials. This figure depicts that as the “A” increases, the wear rate on all materials also increases [34]. The rate of wear response was described with Archard’s principle which was shown in Eq. 12 [35, 36].

Fig. 4 (a–c). Wear rate of materials at various applied loads (a) 0.5 m/s, (b) 1.0 m/s, (c) 1.5 m/s



$$\frac{\text{Wear Volume}}{\text{Sliding Distance}} = K \frac{\text{Applied Load}}{\text{Vickers Hardness}} \quad (12)$$

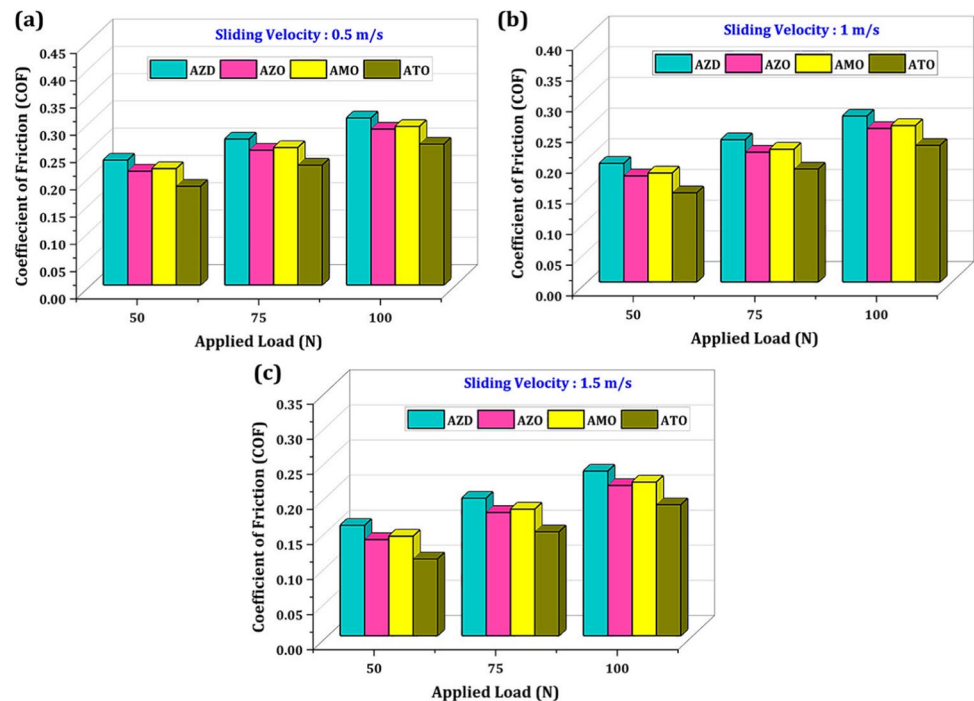
where K is Archard's constant.

The data presented in Fig. 4(a–c) demonstrates that the AZD alloy exhibits a high wear rate under all sliding conditions. This is attributed to the material's softness and weak grain structure, making it susceptible to plastic deformation [37]. In contrast, the metal oxide-reinforced nanocomposites show a lower wear rate than AZD alloy in all conditions. The addition of oxide particles strengthens the matrix and creates cohesive forces between the counter face and the reinforcing particles, leading to strain hardening and reduced wear rate [38]. Among the nanocomposites, the ATO nanocomposite displays the highest wear resistance due to the formation of a thick oxide film on the pin surface, which reduces the material removal rate. The β -Mg₁₇Al₁₂ phase in the AZD alloy dissolves during the T4 heat treatment but is reformed during the T6 heat treatment, contributing to increased wear resistance [36]. Kumar et al. revealed that β -Mg₁₇Al₁₂ contributes to increased wear resistance [39]. Initially, at 50 N, all materials exhibit the minimum wear rate, attributed to less metal-to-metal surface interaction and contact pressure between the pin and disc surface, resulting in lower plastic deformation. However, as the load "A" is increased, the wear rate also increases due to higher contact pressure and material loss in all fabricated materials. A further increase in load to 75 N leads to even higher wear rates in all "B" (0.5–1.5 m/s), caused by the elevated contact pressure between the pin and the counter surface. During this test, wear debris is

left behind by the working samples, and under high pressure, the debris removes any excess material from the interface. As the load increases, the stress on the pin surface also increases, leading to severe abrasion and material removal through micro-cutting. When the load "A" reaches 100 N, the wear rate reaches its maximum under all sliding velocities ("B" values of 0.5–1.5 m/s), owing to increased contact pressure and frictional force between pin-disc material [40]. The rough asperities on the counter face cause direct abrasion and plowing action, resulting in material removal from the pin surface. Under dry sliding conditions, all proposed materials exhibit abrasion wear. However, nanocomposites containing metal oxide particles (AZO, AMO, and ATO) demonstrate superior defense against wear induced by abrasion. The nano-oxide reinforcement enhances wear resistance by developing an oxide layer at the contact surface between the counter and pin material. This layer acts as a protective shield, reducing the impact of hard asperities and lowering the wear rate [41]. Notably, "ATO" displays high wear resistance in all conditions due to its strong interfacial bond with the matrix, reinforcing the oxide layer during sliding.

The COF of all materials under varied "A" factors is shown in Fig. 5(a–c). The AZD alloy has a higher COF than any of the composites at varying "B" values. The COF shows a direct proportionality to the applied load "A," indicating that as "A" increases, the COF also increases [42]. This trend can be seen in both the alloy and nanocomposites. The rise in COF with increasing "A" can be attributed to the higher frictional force experienced when a heavier load is applied. This increased frictional force leads to higher temperatures

Fig. 5 (a–c). COF of materials at various applied loads (a) 0.5 m/s, (b) 1.0 m/s, (c) 1.5 m/s



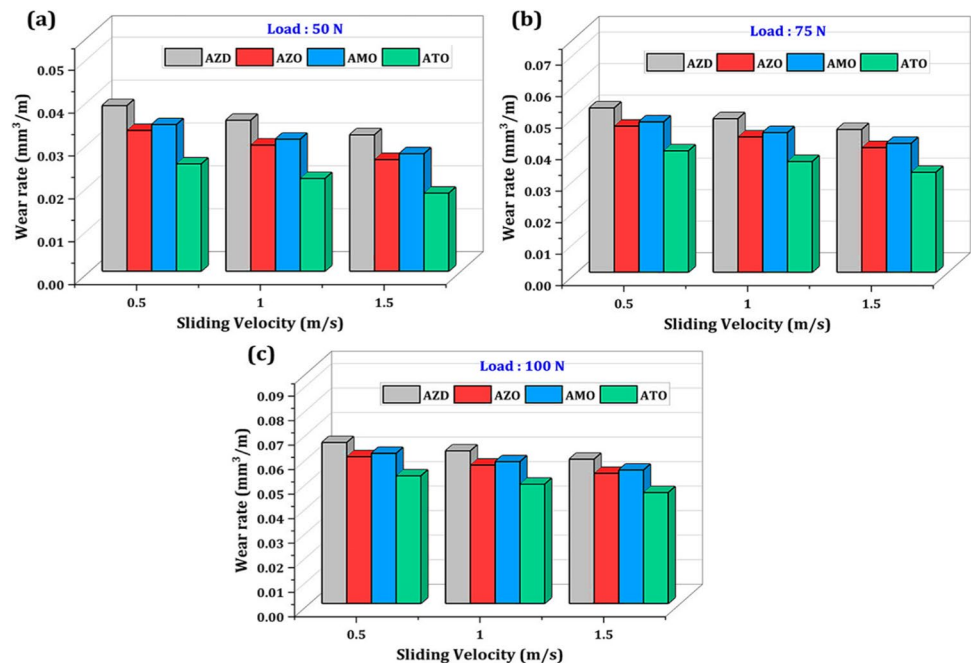
at the interface between the pin and counter plate materials, contributing to a higher COF. The interface's reduced stability due to elevated temperatures results in plastic deformation, weakening the matrix and further increasing the COF. In all "A" conditions, the COF of the AZD alloy remains high, likely because of the soft nature of the Mg alloy, which tends to adhere or stick to the harder counter material. In contrast, the metal oxide-reinforced nanocomposites exhibit lower friction coefficients when compared to the AZD alloy in all conditions. This improvement can be attributed to the incorporation of oxide particles, which reduce the frictional heat generated at the pin and counter-face interface. Among the nanocomposites, the ATO nanocomposite displays the lowest friction due to the combined effect of the oxide layer and a thin tribo-layer. At a load of 50 N, all materials show the minimum COF when compared to other "A" values. This is because the reduced metal-to-metal surface interaction leads to lower frictional force between the pin and disc surface, resulting in less plastic deformation of the materials. However, as the "A" increases, the COF of the materials also increases. This is due to the higher frictional force experienced under heavier loads, leading to a rise in contact temperature at the pin-counter face interface and, subsequently, an elevated COF. The same trend is observed for all nanocomposites. The elevated frictional force results in a rise in temperature at the interface amid the counter face and the pin material, causing the interface to become less stable. Consequently, rapid plastic deformation occurs, leading to a reduction in the matrix's strength and an increase in friction. Additionally, the type of reinforcements used in the nanocomposites also influences their COF [35].

3.2 Effect of sliding velocity on wear rate and COF

Figure 6(a–c) illustrates the wear rate of the fabricated alloy and nanocomposites at "B" under three different "A" of 50, 75, and 100 N. It is observed that as the sliding speed increases, the wear rate decreases. Furthermore, increasing the applied load "B" raises the contact temperature, leading to oxidation on the pin surface, which, in turn, reduces the material loss and reforms the pin-disc tribo-layer [43]. At 0.5 and 1 m/s, all materials exhibit relatively higher wear rates. This can be attributed to the prolonged contact time between the counter face and the test materials, leading to increased frictional force and consequent reduction in material strength [36]. However, at a higher sliding speed of 1.5 m/s, the wear rate of all materials is reduced. The surfaces of the materials oxidize at this higher sliding speed, resulting in the deposition of MgO on the sample surface. This layer acts as a protective barrier between the pin and the counter material, reducing wear [44, 45]. Additionally, the work-hardening effect at higher sliding speeds enhances the material's hardness, further minimizing the wear rate. The increased contact temperature at higher sliding speeds also induces material oxidation, which forms a protective lubricating layer between the pin and disc, guarding the sample from deterioration [46]. Consequently, the material removal rate decreases as "B" increases.

From Fig. 6, it is evident that the AZD alloy exhibits a high wear rate at all "B." This is attributed to the lesser formation of oxidation on its surface. As a result, the AZD alloy demonstrates a higher potential for abrasive wear compared to all the fabricated materials. However,

Fig. 6 (a–c). Wear rate of materials at various sliding velocities (a) 50 N, (b) 75 N, (c) 100 N



the metal oxide-reinforced nanocomposites show lower friction coefficients compared to the AZD alloy in all conditions. The inclusion of oxide particles in these nanocomposites reduces frictional force and aids in the formation of an oxide layer, which protects against rough asperities. Among the nanocomposites, the ATO nanocomposite displays higher wear resistance, mainly due to the presence of Mg_2TiO_3 precipitates and the development of a thin tribolayer.

Figure 7(a–c) shows the COF of the materials at different “*B*.” It indicates that the COF decreases as the “*B*” increases. Initially, at 0.5 m/s, the COF is high due to the dynamic impact between the counter face and the pin surface, resulting in elevated contact temperatures. As a result, the materials become more elastic and softer, leading to higher frictional force at the pin and disc interface. However, as the “*B*” increases from 0.5 to 1 and 1.5 m/s, the COF decreases. This reduction can be attributed to the increase in contact temperature, which induces oxidation (MgO formation) of the materials. The accumulation of MgO serves as a lubricant at the pin-disc interface, reducing the COF. Studies by Chelliah et al. [47] and Banerjee et al. [41] support the notion that the occurrence of this oxide debris on the worn surface contributes to a lower COF. Additionally, the formation of high-contact heat softens the matrix, leading to a decrease in friction, as reported by Aydin et al. [48].

Comparing the COF of the AZD alloy with the nanocomposites shows that the AZD alloy exhibits higher COF at all “*B*.” This can be attributed to the higher heat formation, which weakens the secondary phase and reduces the

grain strength, resulting in an increased material removal rate from the AZD pin surface. In contrast, the addition of oxide particles in the nanocomposites reduces their COF by acting as a protective oxide film on the pin surface and preventing abrasive wear caused by hard asperities. Among all nanocomposites, ATO demonstrates the lowest COF at all “*B*.”

The wear mechanisms of fabricated materials are revealed in Fig. 8a–d. In the case of AZD alloy shown in Fig. 8a, the rate of material removal is high under sliding conditions due to various factors: (i) its soft nature, (ii) lower hardness, (iii) weak interfacial bonding, and (iv) absence of oxide layer formation. Consequently, during repeated loading conditions, the contact pressure between the pin and disc increases, leading to delamination and surface cracks. On the other hand, nanocomposites demonstrate less material loss as depicted in Fig. 8b–d because of the creation of an oxide layer on the sample surface. This layer acts as a lubricant between the pin and disc surfaces, reducing frictional heat. Initially, in composites, the wear rate is high because of the presence of α -Mg. However, after repeated sliding, nanoparticles emerge on the sliding surface and undergo oxidation, forming an oxide film. This film reduces delamination and improves the composite resistance to wear. Particularly, ATO nanocomposite exhibits minimal material loss due to the combined effects of the oxide film and Mg_2TiO_3 precipitates, which effectively reduce frictional heat. Conversely, AMO nanocomposites show higher material loss compared to AZO and ATO nanocomposites due to the weak development of the oxide layer on the sliding surface.

Fig. 7 (a–c). COF of alloy and nanocomposites at various sliding velocities (a) 50 N, (b) 75 N, (c) 100 N

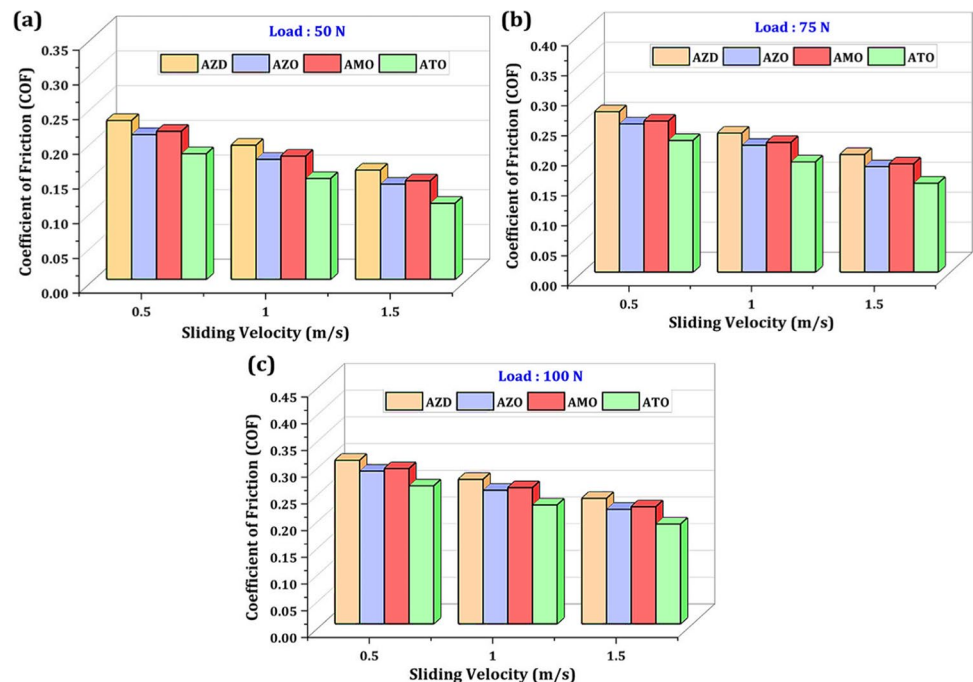
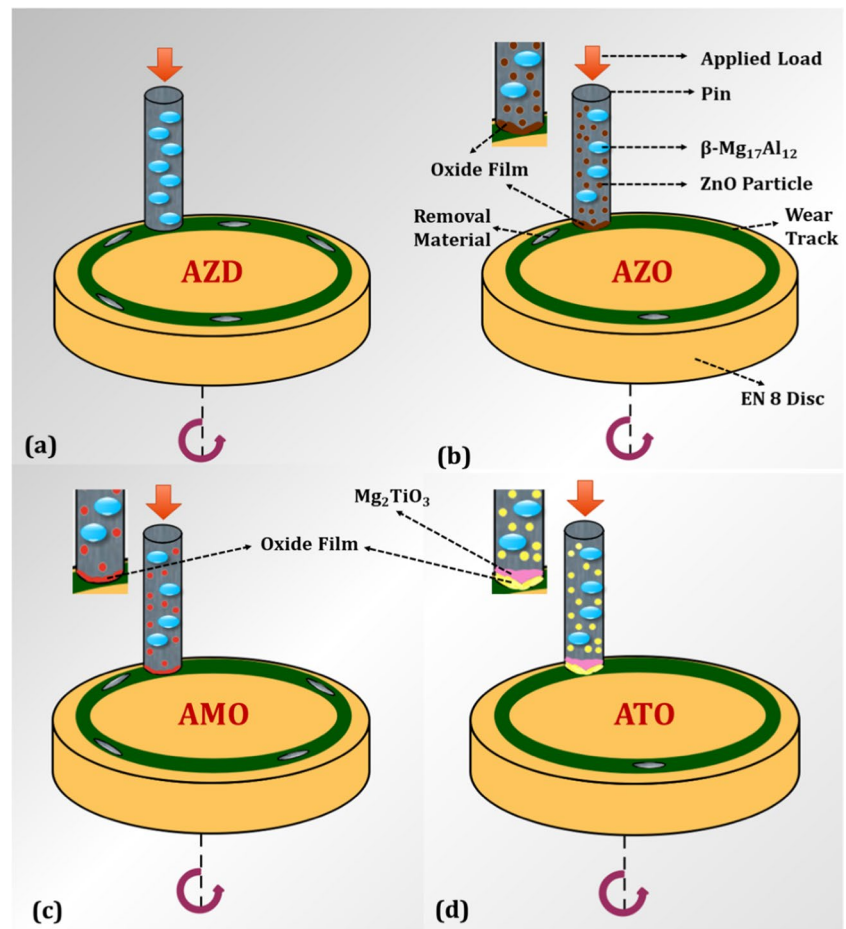


Fig. 8 (a–d). Wear mechanism of all materials

3.3 Worn surface analysis at low and high load condition

The wear mechanisms caused by the effect of “A” (50 N and 100 N) at a constant sliding distance (1000 m) and “B” (1.5 m/s) were examined using SEM, as shown in Fig. 9(a–h). When compared to 100 N, the 50 N “A” pin surface exhibits less material removal due to less contact between the sample and the counter disc. Figure 9(a–d) displays the worn surface of the materials at 50 N. This illustration demonstrated substantial abrasive wear features like deep grooves, micro-cracks, and wear debris. This deep groove was formed by the effect of hard asperities on the soft surface and brittle HCP crystal structure of the Mg alloy matrix [49]. Figure 9(b–d) shows the worn surface of nanocomposites at 50 N. It is demonstrated that the minimum number of grooves and cracks was formed on the nanocomposites. This resulted from the development of a thick oxide layer and MgO, which act as a protective barrier and limit the action of hard asperities on the pin surface. When a significant load is applied, these oxide

particles serve as a load-carrying capacity, reducing wear track peaks and valleys. Among that, ATO composites exhibit fewer scratches and grooves due to the formation of new Mg_2TiO_3 precipitates.

Figure 9(e–h) displays the worn SEM image and wear track of alloy and nanocomposites at 100 N. The worn surface of AZD alloy majorly consists of high delamination and deep grooves as shown in Fig. 9(e). This happened because the AZD alloy’s surface was deeply penetrated by the sharp debris build-up on the EN31 counter material which caused a significant amount of material loss at 100 N. The corresponding wear track of AZD also exhibits high peaks and valleys due to the friction of hard materials over soft ones. The worn surface and wear track of the nanocomposites at 100 N were revealed in Fig. 9(f–h). At the same testing condition, all nanocomposites exhibit minimum grooves and crack formation than AZD alloy. This was caused by the incorporation of oxide particles which reduce the frictional heat between the pin and counter surface. Due to this action, the peaks and valleys of the wear track get reduced.

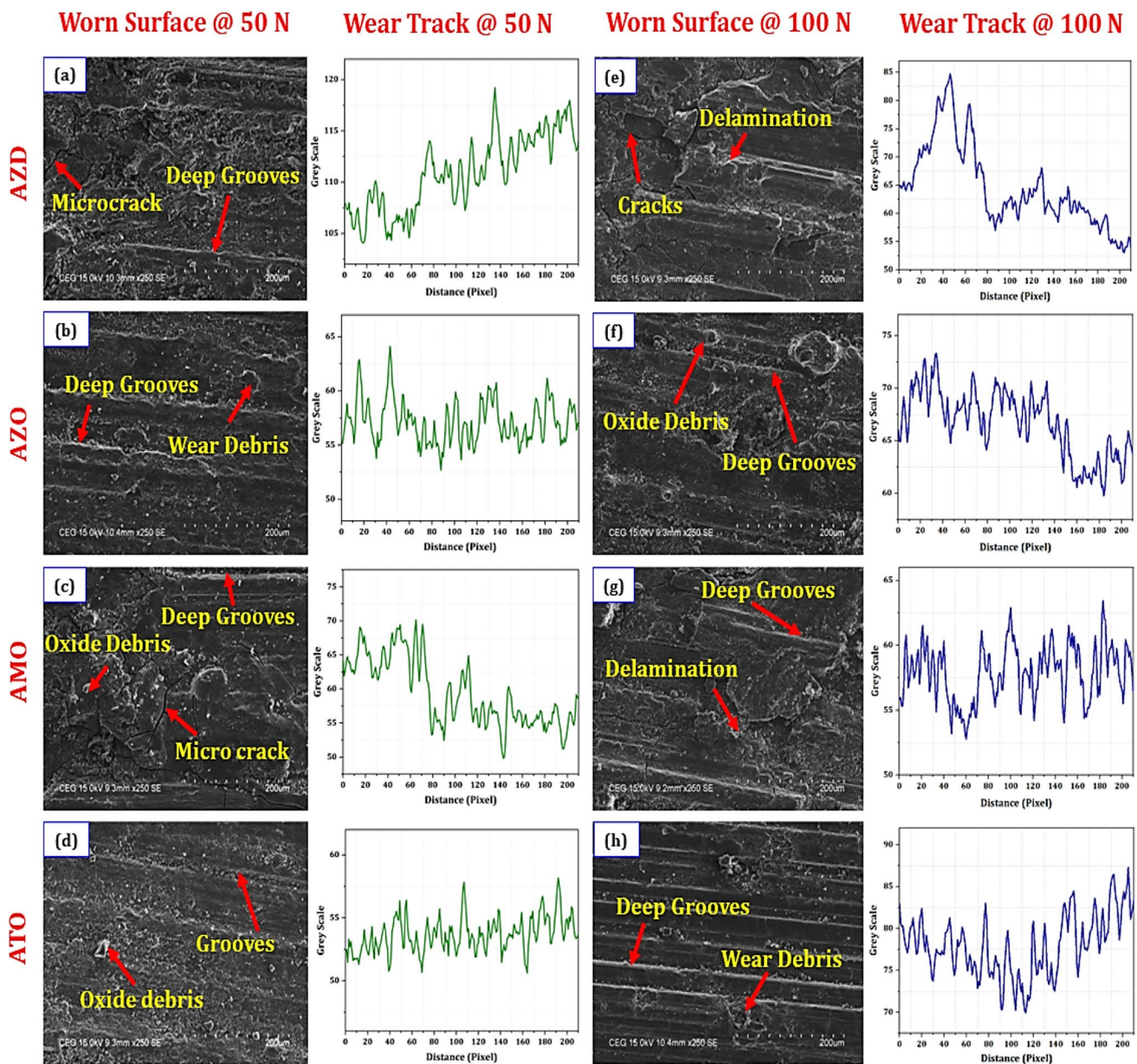


Fig. 9 (a–h). Worn surface and wear track of alloy and nanocomposites at 50 N and 100 N

3.4 Process optimization with EDAS-RSM

The experiments were carried out using an L_{36} OA. The experimental sequence is shown in Table 5. Based on this sequence, experiments were conducted on a pin-on-disc tribometer, and results including wear rate and COF were collected using the weight loss method and DUCOM software. EDAS is one of the multiple criterion decision-making techniques that were utilized to solve multi-response problems. The responses were fed as input into the EDAS technique, and the output of that approach was then sent into

the ANOVA and RSM methods. The initial step of EDAS was computing the positive and negative distances from the average using Eqs. 4 and 6. The calculated PDA and NDA values were then normalized using Eqs. 9 and 10 [29]. The estimated PDA and NDA values as well as the normalized SP and SN are shown in Table 6.

The normalized SP and SN data were averaged to generate the EDAS grade. Table 6 also shows the EDAS grade and the corresponding rank. The 30th trial (“A” = 50 N, “B” = 1.5 m/s, “C” = ATO) generated the highest value of EDAS grade. EDAS grade values correspond to the experimental trials

Table 5 L₃₆ orthogonal experimental sequence and their responses

Exp. No.	Process Parameters			Responses	
	A (N)	B (m/s)	C	Wear rate	COF
1	50	0.5	AZD	0.03862	0.22885
2	50	1	AZD	0.03521	0.19315
3	50	1.5	AZD	0.03181	0.15745
4	75	0.5	AZD	0.05214	0.26748
5	75	1	AZD	0.04874	0.23178
6	75	1.5	AZD	0.04533	0.19608
7	100	0.5	AZD	0.06567	0.3061
8	100	1	AZD	0.06226	0.2704
9	100	1.5	AZD	0.05886	0.23471
10	50	0.5	AZO	0.03284	0.20848
11	50	1	AZO	0.02943	0.17278
12	50	1.5	AZO	0.02603	0.13708
13	75	0.5	AZO	0.04636	0.24711
14	75	1	AZO	0.04296	0.21141
15	75	1.5	AZO	0.03955	0.17571
16	100	0.5	AZO	0.05989	0.28573
17	100	1	AZO	0.05648	0.25003
18	100	1.5	AZO	0.05308	0.21433
19	50	0.5	AMO	0.0342	0.21328
20	50	1	AMO	0.03079	0.17758
21	50	1.5	AMO	0.02739	0.14188
22	75	0.5	AMO	0.04772	0.25192
23	75	1	AMO	0.04432	0.21621
24	75	1.5	AMO	0.04091	0.18053
25	100	0.5	AMO	0.06125	0.29053
26	100	1	AMO	0.05784	0.25483
27	100	1.5	AMO	0.05444	0.21913
28	50	0.5	ATO	0.02502	0.18093
29	50	1	ATO	0.02161	0.14523
30	50	1.5	ATO	0.01821	0.10953
31	75	0.5	ATO	0.03854	0.21956
32	75	1	ATO	0.03514	0.18386
33	75	1.5	ATO	0.03173	0.14816
34	100	0.5	ATO	0.05207	0.25818
35	100	1	ATO	0.04866	0.22248
36	100	1.5	ATO	0.04526	0.18678

as seen in Fig. 10. The calculated EDAS grade values were used for further RSM analysis. The influence of parameters on EDAS was expressed using a second-order polynomial equation, and the model coefficients were calculated using software developed by design experts. For model reduction, backward elimination was utilized, starting by removing higher-order unimportant terms. Equations 13–16 display the regression equation. using coded factors.

$$EDAS(AZD) = 0.854 - 0.009A + 0.2333B + 0.0002A * B - 7.155E - 06A^2 - 0.0041B^2 \quad (13)$$

$$EDAS(AZO) = 0.962 - 0.009A + 0.2307B + 0.000291A * B - 7.155E - 06A^2 - 0.0041B^2 \quad (14)$$

$$EDAS(AMO) = 0.9368 - 0.009A + 0.2317B + 0.000291A * B - 7.155E - 06A^2 - 0.0041B^2 \quad (15)$$

$$EDAS(ATO) = 1.104 - 0.008A + 0.2277B + 0.000291A * B - 7.155E - 06A^2 - 0.0041B^2 \quad (16)$$

3.4.1 ANOVA on EDAS grade

The output of EDAS grade value was utilized as input for ANOVA analysis to determine the most significant process parameter on EDAS grade value and the percentage of contribution to the response. Table 7 displays the ANOVA results for EDAS grade. A confidential level of 95%, or a significance level of 0.05, was used to investigate this analysis. The created model was demonstrated to be relevant with an *F*-value of 87184.73, and the model terms were confirmed to be significant with a *p*-value below the threshold of 0.05. *A*, *B*, *C*, and their interactions (*AB*, *AC*, and *A*²) were all recognized as the key model terms. It can be observed that *A* was the most influential parameter (67.3%) followed by “*B*” (16.8%) and “*C*” (15.8%) which was displayed in Fig. 11. Table 7 shows that the *R*² value (0.9986) of the polynomial model was close to 1. This displays the model’s ability to make predictions about data using actual experimental data. Consequently, this model effectively reflects the link between the independent factors and response (wear rate and COF).

The quadratic mathematical models for EDAS grade values obtained from all experimental trials were validated by analyzing residual plots. Figure 12 presents these plots, which demonstrate the validation of the mathematical models by showing standard normal distributions in the experimental data. The typical residual plots for EDAS grade values consist of the following: actual and predicted EDAS grade values (Fig. 12a), normal percentage probability versus residuals (Fig. 12b), and externally studentized residuals versus predicted EDAS grade

Table 6 Values of PDA, NDA, NSP, NSN, and EDAS grade

Exp. No.	PDA		NDA		NSP	NSN	EDAS Grade	Rank
	Wear rate	COF	Wear rate	COF				
1	0.09741	0.00000	0.00000	0.08556	0.09234	0.91329	0.50282	19
2	0.17710	0.08378	0.00000	0.00000	0.24732	1.00000	0.62366	11
3	0.25656	0.25313	0.00000	0.00000	0.48319	1.00000	0.74159	7
4	0.00000	0.00000	0.21857	0.26880	0.00000	0.50610	0.25305	29
5	0.00000	0.00000	0.13911	0.09946	0.00000	0.75824	0.37912	23
6	0.00000	0.06989	0.05941	0.00000	0.06625	0.93979	0.50302	18
7	0.00000	0.00000	0.53478	0.45200	0.00000	0.00000	0.00000	36
8	0.00000	0.00000	0.45509	0.28265	0.00000	0.25238	0.12619	33
9	0.00000	0.00000	0.37563	0.11336	0.00000	0.50447	0.25223	30
10	0.23249	0.01107	0.00000	0.00000	0.23089	1.00000	0.61545	12
11	0.31219	0.18041	0.00000	0.00000	0.46698	1.00000	0.73349	8
12	0.39165	0.34975	0.00000	0.00000	0.70285	1.00000	0.85143	3
13	0.00000	0.00000	0.08349	0.17218	0.00000	0.74091	0.37046	24
14	0.00000	0.00000	0.00403	0.00283	0.00000	0.99305	0.49653	20
15	0.07567	0.16651	0.00000	0.00000	0.22959	1.00000	0.61479	13
16	0.00000	0.00000	0.39970	0.35537	0.00000	0.23481	0.11741	34
17	0.00000	0.00000	0.32000	0.18603	0.00000	0.48719	0.24360	31
18	0.00000	0.00000	0.24054	0.01668	0.00000	0.73933	0.36966	25
19	0.20071	0.00000	0.00000	0.01170	0.19027	0.98814	0.58920	14
20	0.28040	0.15764	0.00000	0.00000	0.41527	1.00000	0.70763	9
21	0.35986	0.32699	0.00000	0.00000	0.65113	1.00000	0.82557	4
22	0.00000	0.00000	0.11527	0.19499	0.00000	0.68558	0.34279	26
23	0.00000	0.00000	0.03581	0.02560	0.00000	0.93777	0.46888	21
24	0.04389	0.14365	0.00000	0.00000	0.17778	1.00000	0.58889	15
25	0.00000	0.00000	0.43148	0.37814	0.00000	0.17953	0.08977	35
26	0.00000	0.00000	0.35179	0.20880	0.00000	0.43191	0.21595	32
27	0.00000	0.00000	0.27233	0.03945	0.00000	0.68405	0.34202	27
28	0.41525	0.14175	0.00000	0.00000	0.52804	1.00000	0.76402	5
29	0.49495	0.31109	0.00000	0.00000	0.76413	1.00000	0.88207	2
30	0.57441	0.48044	0.00000	0.00000	1.00000	1.00000	1.00000	1
31	0.09928	0.00000	0.00000	0.04149	0.09411	0.95795	0.52603	16
32	0.17874	0.12785	0.00000	0.00000	0.29065	1.00000	0.64532	10
33	0.25843	0.29720	0.00000	0.00000	0.52674	1.00000	0.76337	6
34	0.00000	0.00000	0.21694	0.22469	0.00000	0.55246	0.27623	28
35	0.00000	0.00000	0.13724	0.05534	0.00000	0.80484	0.40242	22
36	0.00000	0.11400	0.05778	0.00000	0.10807	0.94145	0.52476	17

(Fig. 12c). These plots indicate that the residuals and predicted models for EDAS grade in all responses follow a normal distribution. The residuals align closely to the straight line, indicating the normal distribution of random errors. Figure 12a illustrates the agreement between the two responses predicted and actual experimental values, showing good alignment with the measured data. This demonstrates that the generated models for EDAS grade effectively approximate the optimal results. In addition, Fig. 12d displays Pareto charts that illustrate the impact

of process parameters on the wear behavior of the produced composites. A vertical dotted line marked 1.72 represents the critical threshold for a 95% significance level. Effects with absolute values surpassing this threshold (dotted line 1.72) are considered significant. The Pareto analysis confirms the significance of all the examined parameters. Notably, in all cases, the applied load is the major influential element impacting the wear outcomes of the produced MMCs, followed by sliding velocity and materials.

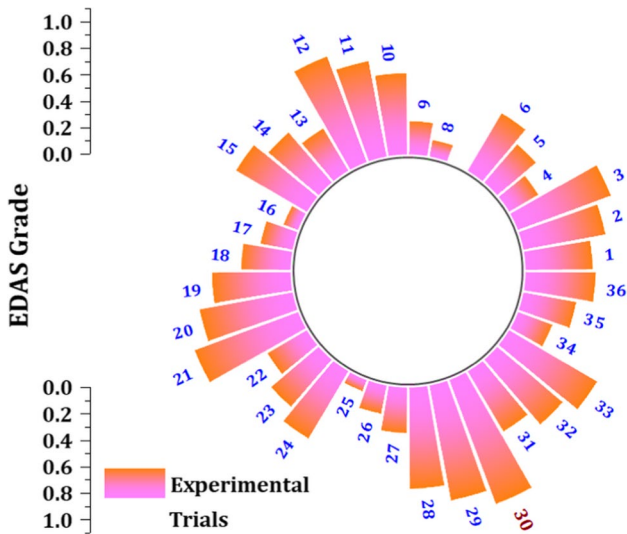


Fig. 10 EDAS values for various trials

3.4.2 Surface plots of EDAS

Figure 13 shows 3D response surface plots developed to analyze the impact of process variables on EDAS. It demonstrates that when the “A” increases, the EDAS values drop in all materials. The value of responses rises as the “A” increases. This was attributed to the increasing load, which increases the frictional force and contact pressure between the pin and counter material surface which increases the heat between them and speeds up the material removal rate. The responses are varied from material to material because of their compositions. When compared to alloys, nanocomposites have higher EDAS values due

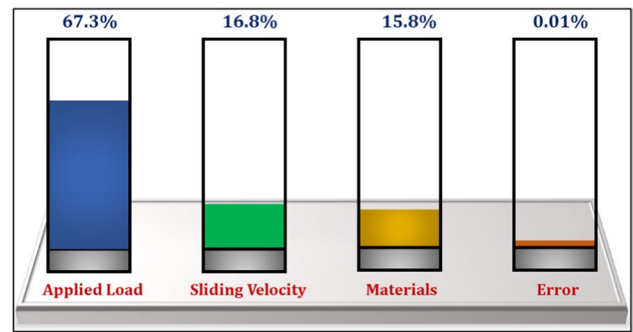


Fig. 11 Effect of various parameters on the responses

to protect the materials from severe damage. Simultaneously, increasing the “B” increases the EDAS value in all materials. Initially, at a minimum sliding speed, the rough asperities of the counter material plow through the matrix material and cause a high amount of material loss. Furthermore, by increasing the sliding speed, the static friction changed into dynamic friction on the material.

3.4.3 Desirability test

The objective of this study was to determine the optimal combination of input parameters for producing nanocomposites with low wear rate and low COF. To achieve this goal, response surface optimization using Design-Expert software was employed, and the results are presented in Fig. 14. Through regression models, the optimal values for the main parameters were determined as follows: parameter “A,” 50 N; parameter “B,” 1.5 m/s; and the use of “ATO” material. These optimal parameter values represent one of the hundred suggestions for achieving the best properties of

Table 7 ANOVA on EDAS grade value

Source	Sum of squares	Degrees of freedom	Mean square	F-value	P-value	Remarks
Model	2.13	14	0.1522	87184.73	< 0.0001	Significant
A—load	1.44	1	1.44	8.243E+05	< 0.0001	
B—sliding velocity	0.3577	1	0.3577	2.049E+05	< 0.0001	
C—material	0.3334	3	0.1111	63655.98	< 0.0001	
AB	0.0002	1	0.0002	121.13	< 0.0001	
AC	0.0002	3	0.0001	36.65	< 0.0001	
BC	0.0000	3	0.0000	6.05	0.0039	
A ²	0.0002	1	0.0002	91.66	< 0.0001	
B ²	8.796E−06	1	8.796E−06	5.04	0.0357	
Residual	0.0000	21	1.746E−06			
Cor total	2.13	35				

R², 0.9986; adjusted R², 0.9814; predicted R², 0.9643; adeq. precision, 1171.9340

to the integration of oxide particles, which limit material deformation and the creation of a thick oxide film

the produced nanocomposites. Figure 14 also displays the desirability values associated with the optimal conditions

Fig. 12 (a-d). (a) Actual vs. Predicted EDAS values, (b) External Studentized Residuals vs. Normal % Probability, (c) Externally Studentized Residuals vs. Predicted, (d) Pareto chart

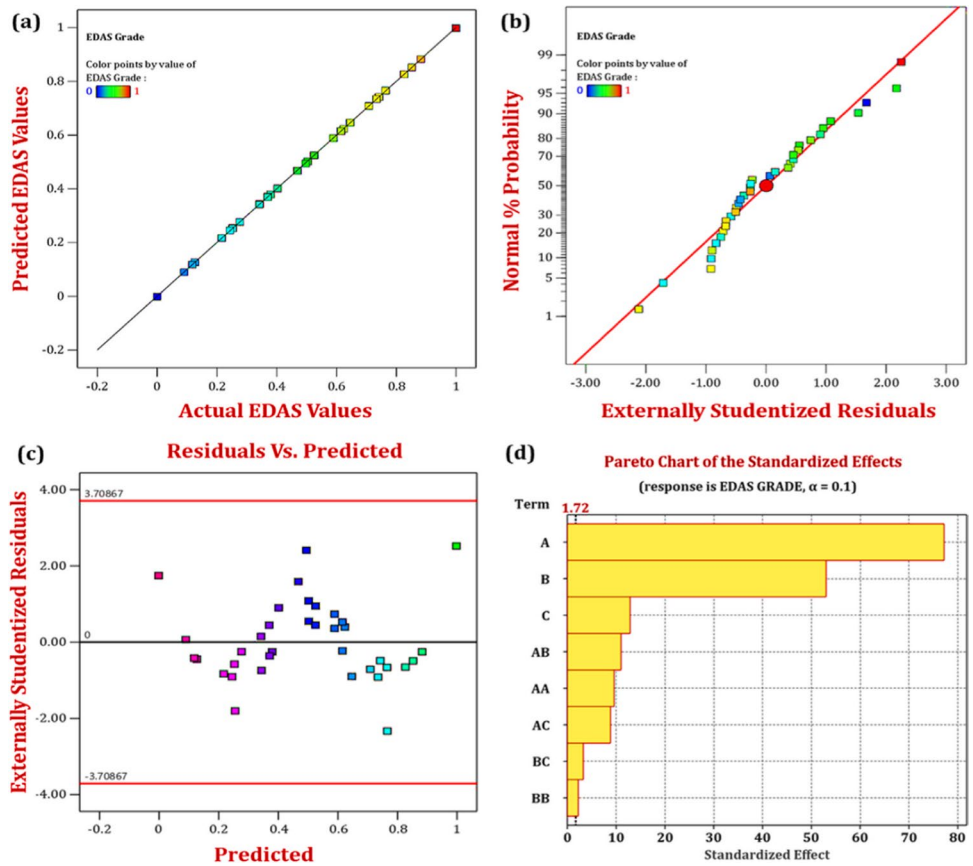


Fig. 13 3D surface plots of EDAS grade

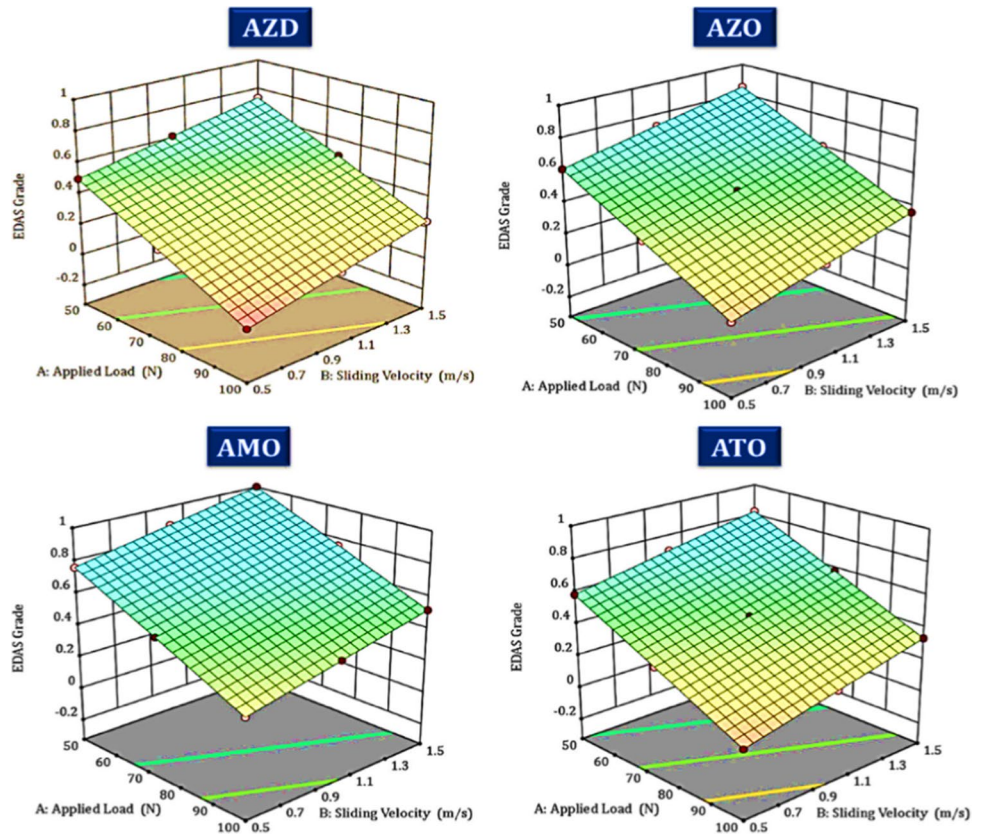
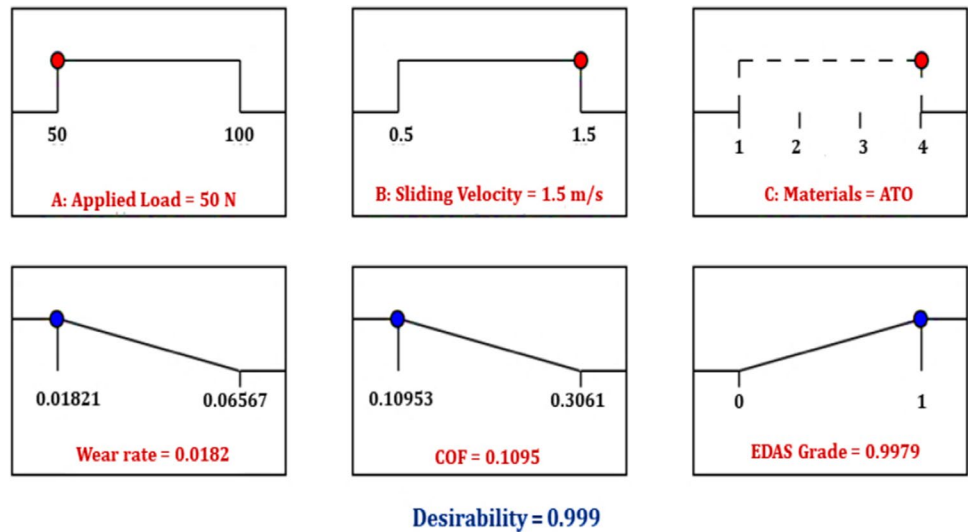


Fig. 14 Desirability graph of process parameter



of the key parameters. Desirability, serving as an objective function, is assigned a range from 0 to 1, where 1 is the target value. The best values for the response variables were determined as follows: wear rate, 0.0182 g/cm³, and COF, 0.1095. Additionally, the EDAS grade value improved to 0.9979, indicating an enhancement in wear resistance.

3.4.4 Confirmation test

Confirmation tests were done to validate the EDAS-accuracy RSMs in predicting optimal values. The initial parameter setting ($A_2B_2C_2$) was made based on the mean EDAS grade. Comparisons were made between the response values obtained from the optimal parameter of the EDAS-RSM and those obtained from the initial parameter. Table 8 lists the outcomes of the confirmation trials and their comparison. During the prediction of the EDAS grade value at the optimum parameter, the EDAS grade value is increased from 0.4965 to 0.9979. When compared to the initial parameter condition, the responses such as wear rate and COF were enhanced by 2.47% and 10.19%, respectively. The confirmation experiments revealed positive outcomes, with significant increases in both the responses and the EDAS grade value.

The findings presented in Fig. 15 demonstrate that under optimal conditions, minimal surface damage was observed in comparison to the initial conditions. Furthermore, the 3D photographs exhibited fewer peaks when optimal conditions were applied. Initially, the elevated surface damage and material removal rate were linked to the simultaneous occurrence of high load and sliding velocity conditions. This resulted in amplified metal contact between the counter and pin surfaces. However, when a load of 50 N was employed under optimal conditions, the wear rate and COF were reduced. This reduction was attributed to the precipitation of a secondary phase and the development of a thick oxide layer, which acted as a protective barrier and reduced material removal rate.

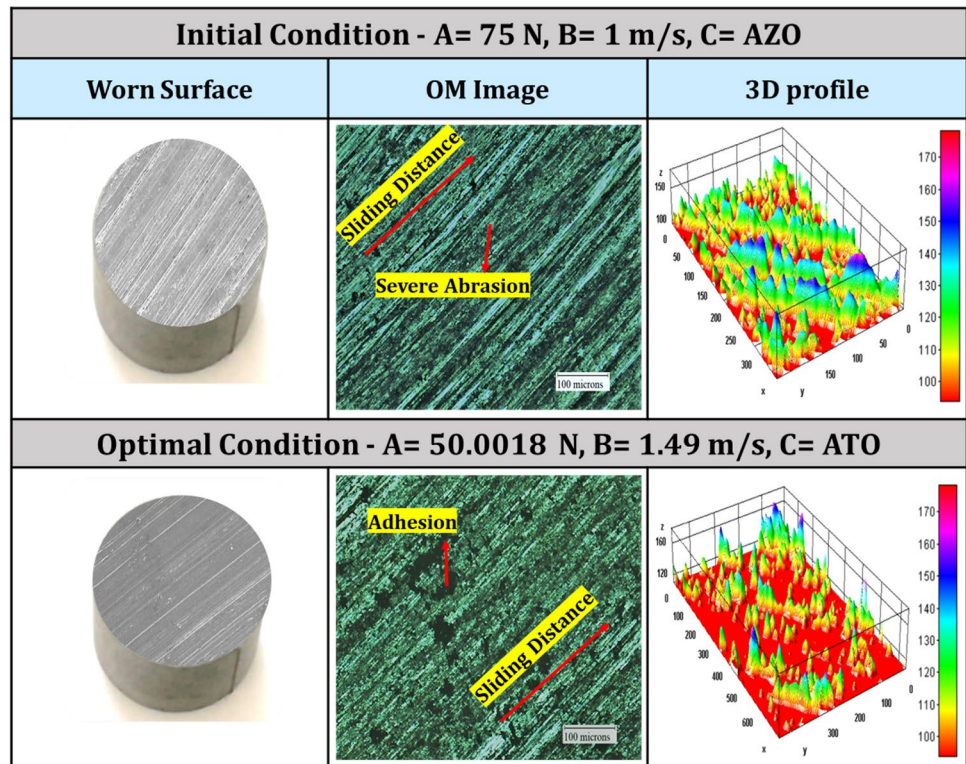
3.5 Effect of temperature on wear and friction at optimized condition

Figure 16 displays the influence of temperature on the material’s COF and wear rate under optimal conditions. The tests were conducted with the optimal parameter values of an “A” of 50 N, “B” of 1.5 m/s, and “C” of ATO at higher working temperatures (50 to 200 °C). It reveals

Table 8 Confirmation test results

Parameter	Initial parameter	Optimal parameters from EDAS-RSM	
		Experimental values	Improvement in the response value
Level	$A_2B_2C_2$	A = 50.0018 N B = 1.4998 m/s C = ATO	
EDAS grade value	0.4965	0.9979	0.5014
Wear rate (mm ³ /m)	0.0429	0.0182	0.0247
COF	0.2114	0.1095	0.1019

Fig. 15 Wear test at initial and optimal conditions



that the ATO nanocomposite's wear rate and COF were continuously raised to 150 °C due to the matrix material's ability to endure temperatures as high as 150 °C without weakening or β -phase dissolution [36]. Additionally, this was caused by the strong interfacial bonding between both the matrix and the oxide reinforcement, which serves as a barrier against plastic deformation. But as the testing temperature is raised, the wear rate and COF rise as a

result of the β -phase dissolving and the grain boundary deteriorating, which weakens the oxide layer and speeds up material removal [50]. When the temperature rises in ATO nanocomposites, the thermal tensions between the oxide reinforcement and Mg matrix rise as well. This leads to the reinforcement particles separating from the grain boundary and increases material loss at higher temperatures.

3.5.1 Worn surface analysis

The worn surface of the ATO material at 150 °C is displayed in Fig. 17(a–d). The SEM images revealed severe delamination and oxidation in all conditions. This delamination is a severe form of wear mechanism that was formed on the surface due to the accumulation of several cracks. Initially, at 50 and 100 °C, the ATO nanocomposite exhibits a lesser amount of material flow and delamination due to the strong secondary phase which acts as a barrier against plastic deformation. Furthermore, an increase in the temperature causes severe wear damage and material flow due to the precipitation weakening and reducing the grain strength.

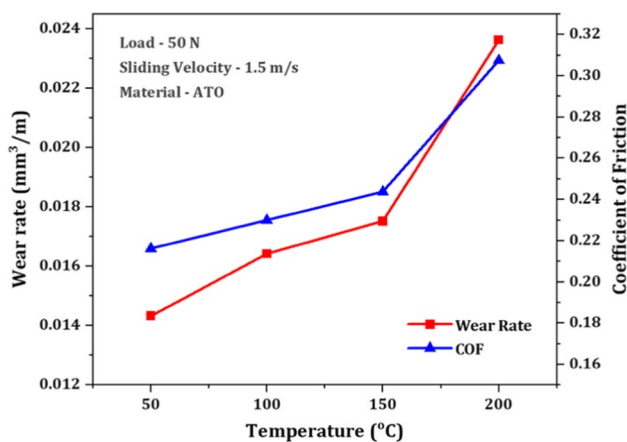
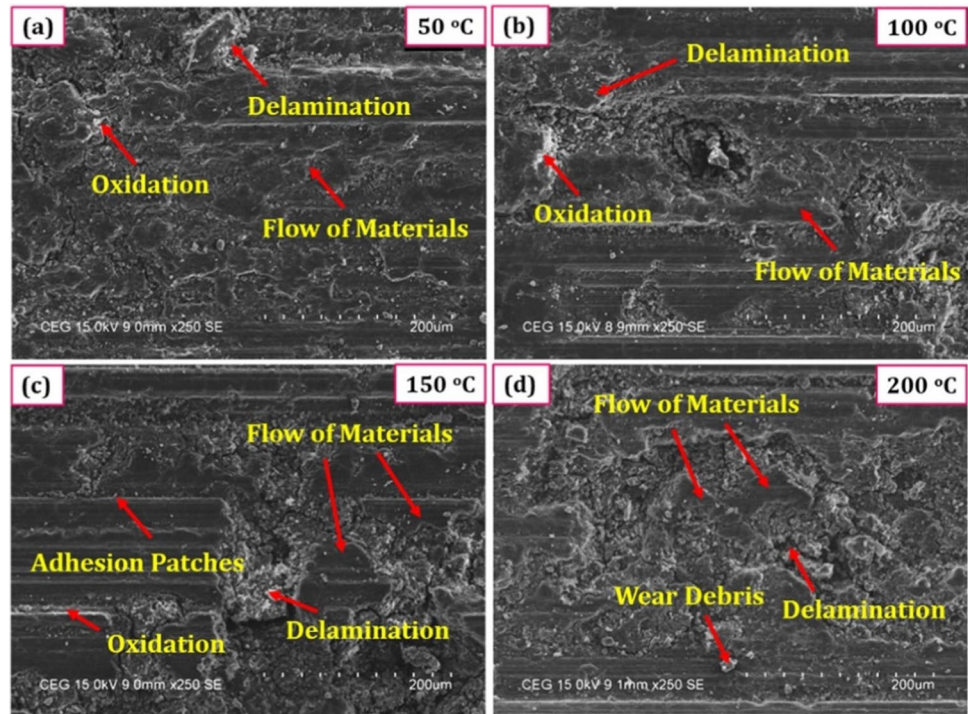


Fig. 16 Temperature effect on tribological properties at optimal conditions

4 Conclusions

The fabrication of AZ91D Mg alloy and its nanocomposites was accomplished through the application of the stir-ultrasonication-squeeze casting technique. To assess

Fig. 17 (a-d). Worn surface of ATO nanocomposite at various elevated temperatures (a) 50 °C, (b) 100 °C, (c) 150 °C, (d) 200 °C



the material's tribological behavior, a pin-on-disc tribometer with an L_{36} orthogonal array was employed. The EDAS-RSM technique was utilized to optimize process variables such as “A” (N), “B” (m/s), and “C” based on wear rate and COF responses. The following conclusions are given below:

1. The tribological characteristics of nanocomposites are enhanced by the incorporation of metal oxide particles. In dry conditions, the wear rate of nanocomposites such as AZO, AMO, and ATO increased by approximately 22.20, 13.89, and 42.75% when compared to AZD alloy. The wear mechanism such as abrasions, delamination, and microscratches was seen in all materials at ambient conditions.
2. The EDAS grade value was used to reduce the multi-answer problem to a single response value. The 30th experiment ($A_1B_3C_3$) yielded the highest EDAS grade (1.000). The R^2 value (0.9986) was quite near to one. This displays the model's ability to make predictions about data using actual experimental data.
3. The ANOVA findings showed that all of the parameters, including “A,” “B,” and “C,” significantly affected the responses. The interactions between the variables AB , AC , and A^2 were also demonstrated by the ANOVA to be significant. Among those “A” process parameters, 67.3% have an impact on the responses.
4. Contour and 3D surface plots displayed the impact of individual process variables on the EDAS grade value. Wear rate and COF increase with increasing “A” and decrease with increasing “B.” Better responses were achieved at an “A” of 50 N, “B” of 1.5 m/s, and ATO material.
5. Using the EDAS-RSM algorithm, the following settings were found to be optimal: an “A” of 50.008 N, a “B” of 1.49 m/s, and a “C” of ATO. The optimum response values were $0.0182 \text{ mm}^3/\text{m}$ wear rate and 0.1095. The confirmation test showed that the EDAS grade had improved by 0.5014.
6. Under optimal conditions, ATO nanocomposites exhibit an abrupt rise in wear rate and COF at temperatures above 150 °C as a result of the degradation of grain strength and dissolving of the secondary phase. In worn surfaces, delamination, wear debris, and oxidation have been observed.

Acknowledgements The authors are thankful to the Science and Engineering Research Board (SERB), India, for funding this research (Grant number: EEQ/2017/000382).

Author contribution A. G.: investigation, data collection, writing, editing, and visualization. E. V.: conceptualization, investigation, writing, and review. N. S. R.: investigation, writing, review, supervision, and project administration. M. P.: writing and review

Funding Open access funding provided by University of Johannesburg.

Data availability The raw/processed data required to reproduce these findings cannot be shared at this time as the data also forms part of an ongoing study.

Declarations

Ethics approval Not applicable

Consent to participate Not applicable

Consent for publication The author confirms that the publication of this paper has been approved by all co-authors and its publication has been approved by the responsible authorities at the institution where the work is carried out.

Competing interests The authors declare no competing interests.

Open Access This article is licensed under a Creative Commons Attribution 4.0 International License, which permits use, sharing, adaptation, distribution and reproduction in any medium or format, as long as you give appropriate credit to the original author(s) and the source, provide a link to the Creative Commons licence, and indicate if changes were made. The images or other third party material in this article are included in the article's Creative Commons licence, unless indicated otherwise in a credit line to the material. If material is not included in the article's Creative Commons licence and your intended use is not permitted by statutory regulation or exceeds the permitted use, you will need to obtain permission directly from the copyright holder. To view a copy of this licence, visit <http://creativecommons.org/licenses/by/4.0/>.

References

1. Staiger MP, Pietak AM, Huadmai J, Dias G (2006) Magnesium and its alloys as orthopedic biomaterials: a review. *Biomaterials* 27:1728–1734. <https://doi.org/10.1016/j.biomaterials.2005.10.003>
2. Nayak S, Bhushan B, Jayaganthan R, Gopinath P, Agarwal RD, Lahiri D (2016) Strengthening of Mg based alloy through grain refinement for orthopaedic application. *J Mech Behav Biomed Mater* 59:57–70. <https://doi.org/10.1016/j.jmbbm.2015.12.010>
3. Su J, Teng J, Xu Z, Li Y (2022) Corrosion-wear behavior of a biocompatible magnesium matrix composite in simulated body fluid. *Fricion* 10:31–43. <https://doi.org/10.1007/s40544-020-0361-8>
4. Kumar K, Das A, Prasad SB (2023) Effect of multi-pass friction stir processing on mechanical, microstructural, bioactivity, and corrosion properties of novel magnesium-hopeite composite for biomedical applications. *Mater Today Commun* 35:105584. <https://doi.org/10.1016/j.mtcomm.2023.105584>
5. Kovacevic S, Ali W, Martínez-Pañeda E, LLorca J (2023) Phase-field modeling of pitting and mechanically-assisted corrosion of Mg alloys for biomedical applications. *Acta Biomater* 164:641–658. <https://doi.org/10.1016/j.actbio.2023.04.011>
6. Song G (2007) Control of biodegradation of biocompatible magnesium alloys. *Corros Sci* 49:1696–1701. <https://doi.org/10.1016/j.corsci.2007.01.001>
7. Hou J, Zhao N, Zhu S (2011) Influence of cutting speed on flank temperature during face milling of magnesium alloy. *Mater Manuf Process* 26:1059–1063. <https://doi.org/10.1080/10426914.2010.536927>
8. Shen J, Li S, Zhai D, Wen L, Liu K, Dai Y (2013) Effects of SiC on the strengthening activated tungsten inert gas (SA-TIG) welded of magnesium alloy. *Mater Manuf Process* 28:1240–1247. <https://doi.org/10.1080/10426914.2013.840907>
9. Li J, Jiang XQ (2011) Effect of cryogenic treatment on the microstructure and mechanical properties of AZ31 magnesium alloy. *Mater Sci Forum* 686:53–56. <https://doi.org/10.4028/www.scientific.net/MSF.686.53>
10. Venkateswarlu K, Saurabh S, Rajinikanth V, Sahu RK, Ray AK (2010) Synthesis of TiN reinforced aluminium metal matrix composites through microwave sintering. *J Mater Eng Perform* 19:231–236. <https://doi.org/10.1007/s11665-009-9458-y>
11. Brar HS, Wong J, Manuel MV (2012) Investigation of the mechanical and degradation properties of Mg-Sr and Mg-Zn-Sr alloys for use as potential biodegradable implant materials. *J Mech Behav Biomed Mater* 7:87–95. <https://doi.org/10.1016/j.jmbbm.2011.07.018>
12. Banerjee S, Poria S, Sutradhar G, Sahoo P (2019) Dry sliding tribological behavior of AZ31-WC nano-composites. *J Magnes Alloy* 7:315–327. <https://doi.org/10.1016/j.jma.2018.11.005>
13. Qasim ZS, Jabbar MA, Hassan JJ (2017) Enhancement of the mechanical properties of aluminum casting alloys (A356) by adding nanorods structures from zinc oxide. *J Mater Sci Eng* 06:2–5. <https://doi.org/10.4172/2169-0022.1000328>
14. El-Mahallawi IS, Shash AY, Amer AE (2015) Nanoreinforced cast Al-Si alloys with Al₂O₃, TiO₂ and ZrO₂ nanoparticles. *Metals (Basel)* 5:802–821. <https://doi.org/10.3390/met5020802>
15. Gu X, Yue J, Li L, Xue H, Yang J, Zhao X (2015) General synthesis of MnOx (MnO₂, Mn₂O₃, Mn₃O₄, MnO) hierarchical microspheres as lithium-ion battery anodes. *Electrochim Acta* 184:250–256. <https://doi.org/10.1016/j.electacta.2015.10.037>
16. Selvam B, Marimuthu P, Narayanasamy R, Anandkrishnan V, Tun KS, Gupta M, Kamaraj M (2014) Dry sliding wear behaviour of zinc oxide reinforced magnesium matrix nano-composites. *Mater Des* 58:475–481. <https://doi.org/10.1016/j.matdes.2014.02.006>
17. Liu X, Zhang Z, Le Q, Bao L (2016) The effects of ZnO particles on the grain refinement and mechanical properties of AZ31 magnesium alloys. *Trans Indian Inst Metals* 69:1911–1918. <https://doi.org/10.1007/s12666-016-0850-7>
18. Panchal HN, Rao VJ (2022) Fabrication of in situ aluminium matrix composite by change in addition sequence of MnO 2 particles. *Eng Res Express* 4:025046. <https://doi.org/10.1088/2631-8695/ac78c7>
19. Jojith R, Radhika N (2019) Mechanical and tribological properties of LM13/TiO₂/MoS₂ hybrid metal matrix composite synthesized by stir casting. *Part Sci Technol* 37:566–578. <https://doi.org/10.1080/02726351.2017.1407381>
20. Ramesh CS, Khan ARA, Ravikumar N, Savanprabhu P (2005) Prediction of wear coefficient of Al6061-TiO₂ composites. *Wear* 259:602–608. <https://doi.org/10.1016/j.wear.2005.02.115>
21. Alagarsamy SV, Ravichandran M (2019) Investigations on tribological behaviour of AA7075-TiO₂ composites under dry sliding conditions. *Ind Lubr Tribol* 71:1064–1071. <https://doi.org/10.1108/ILT-01-2019-0003>
22. Kumar BVM, Basu B, Murthy VSR, Gupta M (2005) The role of tribochemistry on fretting wear of Mg–SiC particulate composites. *Compos Part A Appl Sci Manuf* 36:13–23. <https://doi.org/10.1016/j.compositesa.2004.06.032>
23. Suneesh E, Sivapragash M (2018) Comprehensive studies on processing and characterization of hybrid magnesium composites. *Mater Manuf Process* 33:1324–1345. <https://doi.org/10.1080/10426914.2018.1453155>
24. Wang F, Zhao M (2016) Simulation of particle deposition behavior in cold-sprayed Mg anticorrosion coating. *Mater Manuf Process* 31:1483–1489. <https://doi.org/10.1080/10426914.2014.952042>
25. Gnanavelbabu A, Vinothkumar E, Ross NS, Gupta MK, Jamil M (2023) Tribo-corrosive wear and mechanical properties of nanoparticles reinforced Mg-AZ91D composites. *Tribol Int* 178:108054. <https://doi.org/10.1016/j.triboint.2022.108054>
26. Chen Q, Li K, Liu Y, Zhao Z, Tao K, Zhu Q (2017) Effects of heat treatment on the wear behavior of surfacing AZ91 magnesium

- alloy. *J Mater Res* 32:2161–2168. <https://doi.org/10.1557/jmr.2017.186>
27. Chen G, Yang M, Jin Y, Zhang H, Han F, Chen Q, Zhao Z (2019) Ultrasonic assisted squeeze casting of a wrought aluminum alloy. *J Mater Process Technol* 266:19–25. <https://doi.org/10.1016/j.jmatprotec.2018.10.032>
 28. Shah KB, Kumar S, Dwivedi DK (2007) Aging temperature and abrasive wear behaviour of cast Al–(4%,12%,20%)Si–0.3% Mg alloys. *Mater Des* 28:1968–1974. <https://doi.org/10.1016/j.matdes.2006.04.012>
 29. Zhang S, Gao H, Wei G, Wei Y, Wei C (2019) Evaluation based on distance from average solution method for multiple criteria group decision making under picture 2-tuple linguistic environment. *Mathematics*. 7:243. <https://doi.org/10.3390/math7030243>
 30. Chairman CA, Ravichandran M, Mohanavel V, Sathish T, Rashedi A, Alarifi IM, Badruddin IA, Anqi AE, Afzal A (2021) Mechanical and abrasive wear performance of titanium di-oxide filled woven glass fibre reinforced polymer composites by using Taguchi and EDAS approach. *Materials (Basel)* 14:5257. <https://doi.org/10.3390/ma14185257>
 31. Madhukar P, Selvaraj N, Rao CSP, Veeresh Kumar GB (2019) Tribological behavior of ultrasonic assisted double stir casted novel nano-composite material (AA7150-hBN) using Taguchi technique. *Compos Part B Eng* 175:107136. <https://doi.org/10.1016/j.compositesb.2019.107136>
 32. Singh S, Chauhan NR (2022) Optimization of adhesive wear behaviour of B4C/AZ91D-Mg composites. *Adv Mater Process Technol* 4:4058–4072. <https://doi.org/10.1080/2374068X.2022.2036585>
 33. Rajmohan T, Vijaybhaskar S, Vijayan D (2020) Multiple performance optimization in wear characteristics of Mg–SiC nanocomposites using grey-fuzzy algorithm. *Silicon* 12:1177–1186. <https://doi.org/10.1007/s12633-019-00196-4>
 34. Lu D, Jiang Y, Zhou R (2013) Wear performance of nano-Al₂O₃ particles and CNTs reinforced magnesium matrix composites by friction stir processing. *Wear* 305:286–290. <https://doi.org/10.1016/j.wear.2012.11.079>
 35. Prasad PHD, Radhika N (2020) Comparative study of microstructure, mechanical and reciprocating wear properties of unmodified and Sr-modified A383 alloy and composite. *Trans Indian Inst Metals* 73:1939–1950. <https://doi.org/10.1007/s12666-020-02009-4>
 36. Sunu Surendran K, Gnanavelbabu A (2021) Tribological behaviour of AZ91D/ultra-high-temperature ceramic composites at room and elevated temperatures. *Proc Inst Mech Eng Part J J Eng Tribol* 9:1855–1870. <https://doi.org/10.1177/13506501211010035>
 37. Ramkumar KR, Sivasankaran S, Al-Mufadi FA, Siddharth S, Raghu R (2019) Investigations on microstructure, mechanical, and tribological behaviour of AA 7075–x wt.% TiC composites for aerospace applications. *Arch Civ Mech Eng* 19:428–438. <https://doi.org/10.1016/j.acme.2018.12.003>
 38. Jojith R, Radhika N (2020) Investigation of mechanical and tribological behaviour of heat-treated functionally graded Al-7Si/B4C composite. *Silicon* 12:2073–2085. <https://doi.org/10.1007/s12633-019-00294-3>
 39. Kumar S, Kumar D, Jain J, Hirwani JK (2016) Influence of load, sliding speed, and microstructure on wear response of AZ91 Mg alloy. *Proc Inst Mech Eng Part J J Eng Tribol* 230:1462–1469. <https://doi.org/10.1177/1350650116638601>
 40. Sahoo BN, Panigrahi SK (2019) Development of wear maps of in-situ TiC+TiB₂ reinforced AZ91 Mg matrix composite with varying microstructural conditions. *Tribol Int* 135:463–477. <https://doi.org/10.1016/j.triboint.2019.02.029>
 41. Banerjee S, Poria S, Sutradhar G, Sahoo P (2019) Nanoindentation and scratch resistance characteristics of AZ31–WC nanocomposites. *J Mol Eng Mater* 07:1–13. <https://doi.org/10.1142/s2251237319500072>
 42. Gnanavelbabu A, Gowtham G (2022) Titanium nitride concentration and coordination effect with hexagonal boron nitride enhancing the reciprocating wear behavior of AZ91D alloy-based composites. *Proc Inst Mech Eng Part C J Mech Eng Sci* 237:1463–1485. <https://doi.org/10.1177/09544062221130198>
 43. Ram Prabhu T, Varma VK, Vedantam S (2014) Tribological and mechanical behavior of multilayer Cu/SiC + Gr hybrid composites for brake friction material applications. *Wear*. 317:201–212. <https://doi.org/10.1016/j.wear.2014.06.006>
 44. Seenuvasaperumal P, Elayaperumal A, Jayavel R (2017) Influence of calcium hexaboride reinforced magnesium composite for the mechanical and tribological behaviour. *Tribol Int* 111:18–25. <https://doi.org/10.1016/j.triboint.2017.02.042>
 45. Xiao P, Gao Y, Xu F, Yang C, Li Y, Liu Z, Zheng Q (2018) Tribological behavior of in-situ nanosized TiB₂ particles reinforced AZ91 matrix composite. *Tribol Int* 128:130–139. <https://doi.org/10.1016/j.triboint.2018.07.003>
 46. Gul F, Acilar M (2004) Effect of the reinforcement volume fraction on the dry sliding wear behaviour of Al–10Si/SiCp composites produced by vacuum infiltration technique. *Compos Sci Technol* 64:1959–1970. <https://doi.org/10.1016/j.compscitech.2004.02.013>
 47. Chelliah NM, Singh H, Surappa MK (2016) Correlation between microstructure and wear behavior of AZX915 Mg-alloy reinforced with 12 wt% TiC particles by stir-casting process. *J Magnes Alloy* 4:306–313. <https://doi.org/10.1016/j.jma.2016.09.002>
 48. Aydin F, Sun Y, Emre Turan M (2020) Influence of TiC content on mechanical, wear and corrosion properties of hot-pressed AZ91/TiC composites. *J Compos Mater* 54:141–152. <https://doi.org/10.1177/0021998319860570>
 49. Shanthi M, Nguyen QB, Gupta M (2010) Sliding wear behaviour of calcium containing AZ31B/Al₂O₃ nanocomposites. *Wear* 269:473–479. <https://doi.org/10.1016/j.wear.2010.04.034>
 50. Zafari A, Ghasemi HM, Mahmudi R (2012) Tribological behavior of AZ91D magnesium alloy at elevated temperatures. *Wear* 292:33–40. <https://doi.org/10.1016/j.wear.2012.06.002>

Publisher's Note Springer Nature remains neutral with regard to jurisdictional claims in published maps and institutional affiliations.